MICROROBOTS

Microwheels on microroads: Enhanced translation on topographic surfaces

Tao Yang[1], Andrew Tomaka[1], Tonguc O. Tasci[1]*, Keith B. Neeves[2], Ning Wu[1†], David W. M. Marr[1†]

Microbot locomotion is challenging because of the reversible nature of microscale fluid flow, a limitation that can be overcome by breaking flowfield symmetry with a nearby surface. We have used this strategy with rotating wheel-shaped microbots, microwheels (µwheels), that roll on surfaces leading to enhanced propulsion and fast translation speeds. Despite this, studies to date on flat surfaces show that µwheels roll inefficiently with substantial slip. Taking inspiration from the mathematics of roads and wheels, we demonstrate that µwheel velocities can be significantly enhanced by changing microroad topography. Here, we observe that periodic bumps in the road can be used to enhance the traction between µwheels and nearby walls. Whereas continuous µwheel rotation with slip is observed on flat surfaces, a combination of rotation with slip and nonslip flip occurs when µwheels roll on surfaces with periodic features, resulting in up to fourfold enhancement in translation velocity. The unexpectedly fast rolling speed of µwheels on bumpy roads can be attributed to the hydrodynamic coupling between µwheels and road surface features, allowing nonslip rotation of entire wheels along one of their stationary edges. This road-wheel coupling can also be used to enhance µwheel sorting and separation where the gravitational potential energy barrier induced by topographic surfaces can lead to motion in only one direction and to different rolling speeds between isomeric wheels, allowing one to separate them not based on size but on symmetry.

INTRODUCTION

Microscale propulsion has attracted considerable interest in recent years because of the desire for self-directing in vivo devices (*1*, *2*) and the challenging nature of low Reynolds number flows (*3*). External field-based approaches, especially those using magnetic fields, are among the most promising because they are inherently noncontact and require no chemical fuel. To enable propulsion induced by magnetic torque (*4*, *5*) and without addition of external forces or field gradients, microbot symmetry must be broken either with appropriately designed shape (*6*–*9*) or with proximity to walls (*10*–*20*). However, fabricating asymmetric microdevices of suitable geometry can be challenging, motivating wall-based methods such as microwalkers (*10*), artificial cilia (*11*), microworms (*12*), microcarpets (*13*), microwheels (µwheels) (*14*, *17*), microlassos (*18*), and microswimmer swarms (*15*, *16*, *19*, *20*).

Smooth surfaces, however, are associated with substantial slip with inefficiencies that set the upper limit on translation velocity. Here, we identify surface topographies that register with µwheel structure, taking inspiration from the mathematics of roads and wheels where it can be shown that, for any given wheel shape, there is a complementary road for optimal translation (*21*, *22*). For example, smooth-riding bicycles can be made with square-shaped wheels on roads constructed from a series of truncated catenaries (Fig. 1). Here, we investigate the translation of µwheels of varying size and shape on surfaces designed to mimic their corresponding ideal roads with the goal of enhancing translation velocity. In doing so, we develop methods where wheels of different structure interact differently with different roads, providing opportunities for not only faster devices but also for µwheel separations and sorting, paving the path toward designing micro- and nanodevices capable of enhanced translation, control, and movement within real topographically complex environments.

RESULTS

µWheel translation on flat surfaces

Building on previous work where we have demonstrated that colloidal devices such as pumps and valves can be assembled in two dimensions with external fields (*23*, *24*), we have recently demonstrated that uniform three-dimensional (3D) magnetic fields can create colloid-based µwheels capable of rapid translation on flat surfaces (*14*, *17*). In this, negatively charged superparamagnetic particles of radius a, denser than their surrounding solvent, assembled into close-packed µwheels via isotropic interactions induced by an in-plane rotating magnetic field, $B_{xy}\cos(\omega_M t)\hat{\mathbf{x}} + B_{xy}\sin(\omega_M t)\hat{\mathbf{y}}$, where B_{xy} is the field strength, $\omega_M/2\pi$ is the applied field frequency, and $\hat{\mathbf{x}}$ and $\hat{\mathbf{y}}$ are directional unit vectors (fig. S1). In the studies here, we irreversibly bound µwheel constituent particles together with the addition of positively charged polyelectrolytes [poly(diallyldimethylammonium chloride)] during assembly, yielding a mixture of µwheels of varying size and morphology (Fig. 2A, inset). We characterized these µwheels with the number of constituent particles n and the degree of rotational symmetry ξ.

In the presence of an in-plane rotating magnetic field, fabricated µwheels were laid flat and spun on a surface without net translation; however, upon application of an additional AC field along the z direction, $B_z\cos(\omega_M t + \varphi)\hat{\mathbf{z}}$, where φ is the phase lag between the z and xy components, µwheels stood up and rolled (Fig. 2A and movie S1). Specifically, they inclined relative to the surface and spun in the same plane as the field at a camber angle $\theta_c = \tan^{-1}(B_{xy}/B_z)$. The angular rotational frequency ω of a µwheel is related to the applied angular field frequency ω_M as

$$\omega = \omega_M, \omega_M \le \omega_c$$

$$\omega = \omega_M - \sqrt{{\omega_M}^2 - {\omega_c}^2}, \omega_M > \omega_c \qquad (1)$$

---

[1] Department of Chemical and Biological Engineering, Colorado School of Mines, Golden, CO 80401, USA. [2] Departments of Bioengineering and Pediatrics, University of Colorado Denver, Anschutz Medical Campus, Aurora, CO 80045, USA.
*Present address: BioMEMS Resource Center, Center for Engineering in Medicine and Surgical Services, Massachusetts General Hospital, Harvard Medical School, Boston, MA 02114, USA.
†Corresponding author. Email: ningwu@mines.edu (N.W.); dmarr@mines.edu (D.W.M.M.)

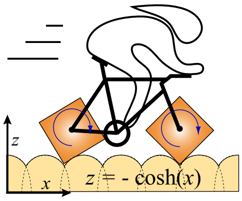

Fig. 1. Square-wheeled bicycles can translate smoothly on roads constructed from truncated catenaries.

where ω_c is the critical frequency related to the overall applied field strength (*25*). In this work, we typically ran experiments with $0.628 \leq \omega_M \leq 314$ rad/s. For 2D disc-like µwheels, the time-averaged translation velocity $\bar{v}$ is proportional to ωR_n, with radius $R_n \propto \sqrt{na}$, leading to $\bar{v}/\omega a \propto \sqrt{n}$. Supporting this scaling, experiments show that larger µwheels rolled faster on flat substrates (Fig. 2B), and µwheels of similar size, such as diamond- and square-shaped tetramers, rolled with similar velocity. We note that the slope of the line in Fig. 2B, $\bar{v}/\omega R_n$, is far from unity (~0.1), indicating substantial slip during rolling, consistent with earlier studies (*14*, *17*).

Because µwheels were assembled from individual spherical colloidal building blocks, their perimeter was not strictly circular. As a result, µwheel translation on flat surfaces was influenced by geometry and the specific manner in which µwheels interacted with the surface. This is seen in Fig. 2C, where the instantaneous velocities of µwheels over one period of rotation demonstrated oscillations inversely proportional with their degree of rotational symmetry. To describe this observation, we modeled the rolling of µwheels of different size and symmetry on flat surfaces by extending the analysis of Tierno *et al.* (*26*, *27*). Although greater detail can be found in the Supplementary Materials, here, we focus on dimers ($n = 2$, $\xi = 2$), whose motion is shown in movie S2 and fig. S2B. In this case, the instantaneous velocities parallel $v(t)$ and perpendicular $v_z(t)$ to the substrate can be written as

$$\frac{v(t)}{V_0} = \frac{dx}{dt} = -\frac{1}{2}(\beta_2 - \beta_1)\cos(\omega t)$$

$$\frac{v_z(t)}{V_0} = \frac{dh}{dt} = \frac{1}{2}(\alpha_2 - \alpha_1)\sin(\omega t) \qquad (2)$$

where x and h are the displacements of a dimer parallel and perpendicular to the substrate based on the center of mass. $V_0 = 4\omega af/3$ is a characteristic velocity, where $f(a/h)$ is a correction factor that accounts for the rotation of a sphere near a wall (*28*–*30*)(see "Modeling for µwheel translation on flat and textured surfaces" section in the Supplementary Materials). β_i and α_i are the hydrodynamic mobilities of lobe i moving parallel and perpendicular to the substrate and are functions of the lobe-wall separation h_i. In our work, because µwheels were very close to the substrate, we used expressions (eq. S3) based on asymptotic lubrication theory (*31*), which provides the correct limits that α_i, $\beta_i \rightarrow 0$ when the contact distance $a/h_i \rightarrow 1$.

We solved Eq. 2 for dimers and plotted the instantaneous velocities in fig. S2 (B and C). In our calculations, we set the initial separation between the µwheel edge and the substrate to $0.2a = 450$ nm determined by balancing the buoyancy force on the µwheel and the electrostatic repulsion between the µwheel and the substrate. We see that $v(t)$ varied with the dimer orientation during rolling and reached a maximum when the dimer stands up and a minimum when it is parallel to the surface. This behavior arises from the difference in the hydrodynamic mobilities ($\beta_1 - \beta_2$) between lobes, which depends on lobe-wall separations h_1 and h_2 (eq. S3). When a dimer is suspended in bulk fluid far away from the substrate, no net translation is expected because their mobilities are equal, $\beta_1 = \beta_2 = 1$; similarly, when a dimer is very close to the substrate but lies parallel with both lobes equally separated from the substrate, v equals 0 because, once again, the mobilities are equal and $\beta_1 = \beta_2 = 0$. When the dimer stands up, however, the difference in mobilities β_i is largest, and the dimer has the greatest speed. Matching µwheel symmetry, the dimer orientation changes twice per rotation as does the velocity. We note that during rotation the µwheel center of mass did not remain a constant distance from the substrate (fig. S2C), rather it oscillated with the same period as its lateral velocity because of differences in mobilities α_i between lobes. Only perfectly circular wheels such as monomers roll with their center-of-mass constant elevation above a flat substrate. Note that over the course of rotation, our modeling predicts only ~0.1a oscillation from the average center of mass to substrate separation, a short distance that explains relatively smooth rolling during dimer translation. This can also be observed by tracking the displacement of the centers of mass of both lobes, which exhibit a characteristic 180° phase difference (fig. S2D). By solving eq. S6 for µwheels with different degrees of symmetry ($2 \leq \xi \leq 6$), we observed similar features in v and v_z. As shown in Fig. 2C,

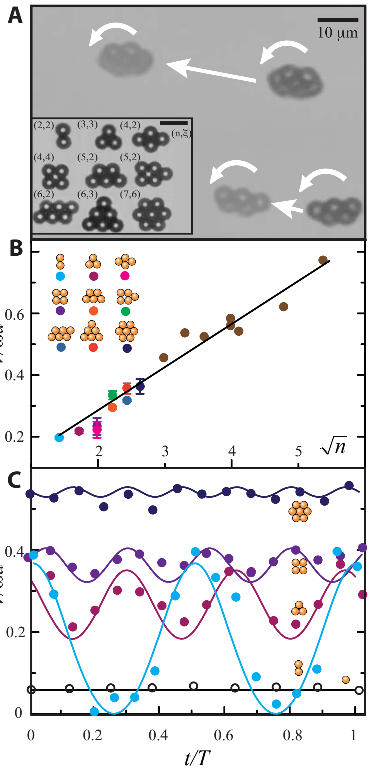

Fig. 2. µWheel translation on flat surfaces. (**A**) A 5-mer (5,2) and a 7-mer (7,6) translate at different velocities in the same applied field. Inset: µWheels of different size ($1 < n < 7$) and symmetry ($2 < \xi < 6$). Scale bars, 10 µm. (**B**) Time-averaged velocity (normalized by the frequency and particle radius) of µwheels of different size ($2 < n < 29$). Brown dots correspond to µwheels with $n > 7$. (**C**) Instantaneous velocity profiles for singlet (1,1), dimer (2,2), trimer (3,3), square (4,4), and 7-mer (7,6) µwheels. Symbols are experimental measurements, and solid lines are calculations based on Eq. 2 and eq. S6, where T is one full rotational period.

predictions for the lateral velocities v correspond to our experimental data.

μWheel translation on periodic topographic surfaces

On flat surfaces, μwheels demonstrate substantial slip (~90%) because the μwheel-wall hydrodynamic interaction weakly contributes to net translation. We improved coupling and increased translation velocities by introducing periodic features on the substrate. In our case, as wheel shape varied, substrate structure could be modified most simply by changing road periodicity and spacing to match wheel features. Ideal substrates for rolling without slip for μwheels of different symmetry can be predicted numerically (Fig. 3A and see Supplementary Materials for details).

To mimic continuous surfaces with repeating catenary features, we fabricated topographic surfaces using polydimethylsiloxane (PDMS) replicas of linear diffraction gratings (Fig. 3B). Experimental measurement by atomic force microscopy (AFM) shows that the spacing between ridges was 9.9 μm, maximum height was 3.83 μm, and blaze angle was $\gamma = 26°$. One of the advantages of this surface is that effective spacings between ridges can be varied by simply changing μwheel rolling angle θ (Fig. 3B). We began with dimers where, by tracking the center of mass of each lobe, we identified two distinct translation modes during rolling (Fig. 3C and movie S3). Mode I occurs when dimers translate between two peaks, during which they rotate along their center of mass, evidenced by the characteristic 180° phase difference between lobes. This mode is the same as observed on flat substrates (fig. S2D) and is associated with weak wheel-surface interaction, substantial slip, and a relatively low net translation velocity. With addition of surface features, however, a second mode, mode II, appears where μwheels approach and flip over peaks. In mode II, the lobe adjacent to the peak remains almost motionless, whereas the other rotates about a full dimer length; essentially, the dimer flips without slip. This is reflected by the almost constant lateral position for the red lobe during mode II in Fig. 3C. As dimers rolled on these periodic surfaces, these two modes alternated effectively via "slip and flip," leading to a faster net translation velocity on patterned surfaces than on flat ones.

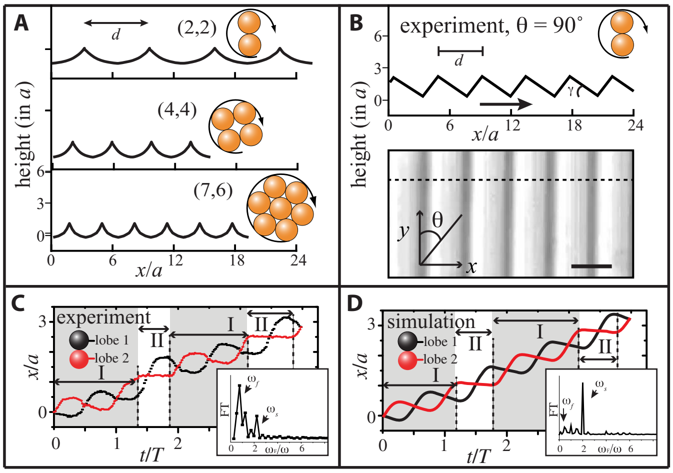

Fig. 3. μWheel translation on topographic surfaces. (**A**) The calculated commensurate "roads" for μwheels of n = (2,2), (4,4), and (7,6) where optimal spacings d are 6.3a, 3.8a, and 3.1a, respectively. (**B**) Experimental geometry (measured by AFM along θ = 90°) with minimum spacing of $d = 4.4a$ and blaze angle of $\gamma = 26°$; spacing can be readily increased by lowering translation angle θ. Maximum height is 1.7a, and arrow indicates blaze direction. Scale bar, 10 μm. (**C**) Experimental measurement of displacement of the centers of mass of two dimer lobes with time rolling along θ ~ 90° against the blaze direction. Mode I, rotation with slip; mode II, nonslip flipping. Insets: Fourier transform of the instantaneous velocity. (**D**) Calculated displacement of the centers of mass of two lobes of a dimer rolling along a textured surface with trapezoidal bumps (fig. S3B). Insets show the Fourier transforms of the instantaneous velocity.

To better understand the slip and flip translation of μwheels on textured surfaces, we again used Eq. 2 but then incorporated surface topography $h_s(x)$ into the mobilities α_i and β_i in eq. S3 via $h_1 = h + a \cos \omega t - h_s(x + a \sin \omega t)$ and $h_2 = h - a \cos \omega t - h_s(x - a \sin \omega t)$, where h_1 (h_2) is the separation between the center of lobe 1 (lobe 2) and the patterned substrate (fig. S3A). We note that this method is an approximation; the calculation of exact sphere mobilities near nonflat surfaces is nontrivial, and only the influence of walls with small-amplitude, sinusoidal deformations has to date been reported (*32*). As a result and instead of modeling the rolling of dimers along surfaces that exactly match our experiments, we used small trapezoidal bumps to represent microroad surface features. As shown by $h_s(x)$ in fig. S3B, the spacing between bumps d was 4.4a, the same as that between gratings in our experiments. The height and length of the bumps were then tuned to be 0.38a and 0.2a, respectively, so that the dimer rolled at the same time-averaged speed as observed in our experiments. The instantaneous velocities parallel (v^p) and perpendicular (v_z^p) to the topographic substrate could then be solved numerically (Eq. 2 and eqs. S3 and S8), and their motion could be shown (movie S4). In Fig. 3D, we plot the lateral displacement of the center of mass of each dimer lobe. We also observed the appearance of the translation mode I slip characterized by a 180° phase difference and mode II flip with almost zero displacement of one lobe (the red line in Fig. 3D). By further examining movie S4, we found that the existence of bumps on the road made lobe 2 (red) contact the bump closely. As a result, its parallel and perpendicular hydrodynamic mobilities were almost zero following lubrication theory (*11*, *30*). Therefore, lobe 2 remained stationary, whereas lobe 1 (black) rotated along lobe 2's center of mass, leading to a flip. Because $\alpha_2, \beta_2 \sim 0$, the difference in mobilities between the two lobes, and hence the translation velocity, is at a maximum during flip. This model reveals that noncircular μwheels could roll faster on appropriate bumpy microroads due to the hydrodynamic coupling and the resulting nonslip flip. Although the sawtooth-like surface topography in our experiments was more complicated, the simplified trapezoidal bumps in our modeling captured the underlying physics. When we set a very small initial separation of 0.05a between the dimer edge and flat substrate in simulations, we observed sequential lobe flips instead of normal rolling (movie S5). This again is due to the marked mobility drop of one lobe that was very close to the substrate, whereas the other lobe simply rotated around it.

The slip and flip modes were also apparent via Fourier transform of the instantaneous μwheel translation velocity v^p (Fig. 3, C and D, insets), where two frequency peaks arose. The first frequency, the slip frequency ω_s, is related to the angular rotational frequency and μwheel symmetry, $\omega_s = \xi\omega$. The second frequency, the flip frequency ω_f, is related to how often a μwheel encounters a surface peak, governed by the surface feature spacing d and μwheel rolling angle θ: $\omega_f = 2\pi\bar{v}^p \sin\theta/d$, where $\bar{v}^p$ is the average μwheel lateral translation velocity on a topographic surface.

With a combination of slip and flip, $\bar{v}^p$ can be expressed as $\bar{v}^p = \frac{\int_0^{\tau_s} v_s dt + \int_0^{\tau_f} v_f dt}{\int_0^{\tau} dt} = \frac{\tau_s}{\tau}\bar{v}_s + \frac{\tau_f}{\tau}\bar{v}_f$, where v_s and v_f, as well as τ_s and τ_f, are the instantaneous translation velocities and periods for the slip and flip motion with $\tau = \tau_s + \tau_f$. Note that τ_f and τ are related to ω_s and ω_f by $\tau_f = 2\pi/\zeta\omega = 2\pi/\omega_s$ and $\tau = 2\pi/\omega_f$. If we define C_s and C_f as the propulsion coefficients for slip and flip, respectively, then $\bar{v}_s = C_s\omega R_n$, $\bar{v}_f = C_f\omega R_n$, and $\bar{v}^p = \omega R_n\left[\left(1-\frac{\omega_f}{\omega_s}\right)C_s + \frac{\omega_f}{\omega_s}C_f\right]$. Recalling that the average µwheel translation velocity on flat surfaces $\bar{v} = C\omega R_n$ (Fig. 2B), the ratio of average translation velocities becomes proportional to ω_f/ω_s as

$$\frac{\bar{v}^p}{\bar{v}} = \left(\frac{C_f}{C} - \frac{C_s}{C}\right)\frac{\omega_f}{\omega_s} + \frac{C_s}{C} \qquad (3)$$

Following Eq. 3, we measured $\bar{v}^p$, ω_s, and ω_f for rolling µwheels of different sizes and symmetries at different rolling angles θ, both along and against the blaze direction (Fig. 4A). We fitted experimental data with Eq. 3 to find $C_f/C = 4.07$, $C_s/C = 0.22$. The ratio $C_s/C < 1$ indicates some deceleration in the flip mode along θ = 0° due to channel edges. The ratio $C_f/C > 1$ indicates that efficient flipping led to roughly fourfold faster net translation velocity on topographic surfaces. By adjusting the spacing between bumps on the microrod, we could completely eliminate the slip mode, allowing the dimer to flip continously as shown in movie S6. Via substitution of Eq. 3, the ratio of ω_s/ω_f becomes

$$\frac{\omega_s}{\omega_f} = \frac{\xi\omega d}{2\pi\bar{v}^p\sin\theta} = \left(\frac{d}{2\pi a C_s}\right)\cdot\frac{\xi}{\sqrt{n}\sin\theta} + \left(\frac{C_f}{C_s} - 1\right) \qquad (4)$$

suggesting a linear relationship between ω_s/ω_f and $\xi/\sqrt{n}\sin\theta$. This was observed experimentally (Fig. 4B), where deviations for 7-mers could be attributed to effectively smaller symmetry degrees. In addition, the bigger slope associated with rolling along the blaze indicates a longer time required to climb inclined surfaces between peaks, a feature not included in our simple model.

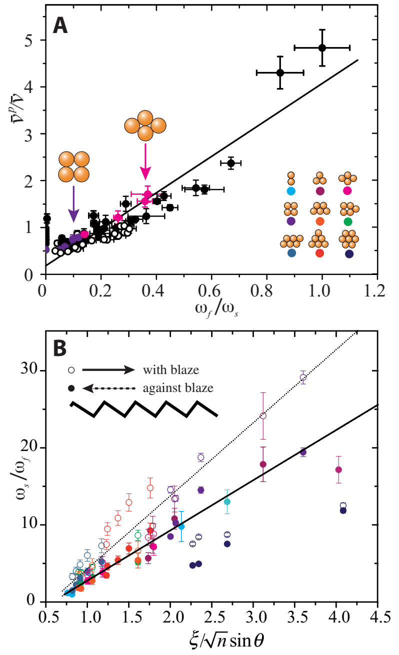

Fig. 4. Enhanced µwheel velocities on topographic surfaces. (**A**) The ratio of topographic to flat surface µwheel average translation velocities $\bar{v}^p/\bar{v}$ with the ratio of spatial/rotational frequency ω_f/ω_s. Open and closed symbols represent with and against the blaze direction. The line is a fit from Eq. 3. (**B**) The dashed line is a fit from Eq. 4 with the blaze, and the solid line is against the blaze direction. Symbols are identical to those of Fig. 2B.

A µwheel "rectifier"

One advantage of constructing surfaces from diffraction gratings is that the surface feature slope is steeper in one direction of travel, the blaze direction, than the other (Fig. 3B), allowing us to investigate the impact of energy barrier on rolling. If the magnetic field frequency is below a critical value, then dimers will be trapped between surface features when rolling against the blaze direction (Fig. 5 and movie S7). If the direction is switched, however, then dimers will translate readily at all field rotation frequencies, a rectifying effect that can be understood by considering the relevant forces (*33*, *34*). For a µwheel rolling along a surface slope with angle γ (Fig. 5A, inset), µwheels experience (i) a translation-rotation coupling hydrodynamic force $F_{d,tr} \sim 6\pi\eta\omega R_n^2$, where η is the solvent viscosity; (ii) a gravitational force $F_g = mg\sin\gamma$, where $m = n\Delta\rho\left({}^4/_3\ \pi a^3\right)$ is the effective µwheel mass; and (iii) a wet friction force $F_f = \mu_k mg\cos\gamma$, where μ_k is the kinetic friction coefficient. The balance between these three forces determines whether a µwheel can overcome the geometric barrier to reach the next surface peak or, if $F_f + F_{d,tr} < F_g$, be trapped. Because $F_{d,tr}$ is proportional to the angular rotational frequency ω, there exists a critical frequency ω* below which the dimer does not translate. By letting $F_f + F_{d,tr} \sim F_g$, we estimated that ω* ~ 3.73 rad/s for dimers rolling along θ = 90° against the blaze direction, close to the experimentally determined value (ω* ~ 3.77 rad/s). In addition, aiding translation here is that the slope length along the blaze direction is shorter than the dimer long axis, allowing it to easily roll over surface peaks without having to overcome the larger gravitational energy barrier (Fig. 5B). For µwheels larger than the slope length in either direction—diamond-shaped tetramers, for example—rectifying disappears because they can translate in either direction at all frequencies. On the other hand, the square-shaped tetramer can only move with the blaze direction at all frequencies.

Separation of isomeric µwheels by symmetry

For a given rotation rate and on flat surfaces, µwheel size is the most important factor in determining velocity, and isomeric µwheels roll at about the same speed; for example, diamond- and square-shaped tetramers translated at similar velocities (Figs. 2A and 6A), and they could not be easily separated from each other. Topographic surfaces, however, could be exploited to separate isomeric µwheels. For example, diamond wheels interacted more effectively with the textured surfaces than squares with $(\omega_f/\omega_s)_{\text{diamond}} > (\omega_f/\omega_s)_{\text{square}}$ (Fig. 4A). With a larger velocity enhancement for diamond µwheels (Fig. 4A), one could

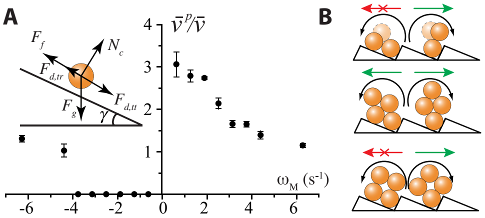

Fig. 5. µWheel rectifying on topographic surfaces. (**A**) The ratio of dimer translation velocities on topographic/flat surface $\bar{v}^p/\bar{v}$ with field frequency. Negative frequencies indicate propulsion direction again the blaze direction. The inset shows the force balance on the µwheel. (**B**) Illustration of the rectifier effect for dimer (2,2), diamond (4,2), and square (4,4) µwheels.

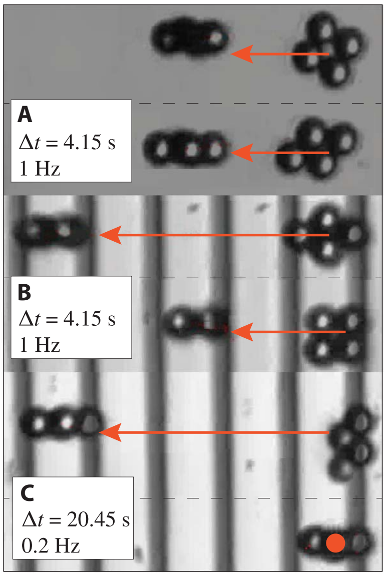

Fig. 6. Separation of µwheel isomers. Composite images of diamond and square µwheels translating on a (**A**) flat surface versus on a (**B**) textured surface (against the blaze direction) with the same time interval under identical field conditions (movie S8). (**C**) A diamond and square translating against the blaze under low magnetic field frequency (movie S9).

separate them from square µwheels by rolling them simultaneously on the same textured surface (Fig. 6B and movie S8). An alternative approach to separate isomers is to take advantage of the rectifier effect and manipulate the applied field frequency because there is a frequency range within which the difference in the change of gravitational energy during rolling between diamond and square wheels is large enough so that diamond wheels translate continuously, whereas square wheels remain stationary (Fig. 6C and movie S9). Our observations are reminiscent of physical methods that rely on geometric constraints, such as arrays of posts or obstacles, to bias the net transport direction of objects of different sizes, including cells and colloids for separations (*35*–*37*). Instead of size, here, we used the coupling between translation speed and symmetry of objects induced by patterned surfaces, offering a new way to separate microscopic objects.

CONCLUSION

We have investigated the rolling of superparamagnetic µwheels of different sizes and symmetries driven by a rotating magnetic field on flat and textured surfaces. On flat surfaces, the overall translation speed of µwheels is governed by their size with substantial slip during rotation. With addition of periodic features on the surface, however, we observe two alternating translation modes, slip and flip, which are tied to surface topography. The flip mode arises because of the hydrodynamic coupling between the textured surface and the µwheel, which allows simple rotation of the whole wheel along one of its stationary edges. Because the flip motion shows no slip, the overall µwheel translation velocity is significantly enhanced. We further demonstrate that the unique propulsion behavior of µwheels on topographic surfaces can be used for separation of isomeric µwheels of different symmetry. The hydrodynamic coupling between textured surfaces and µwheels revealed in our study may lead to more efficient propulsion of microdevices in topographically complex environments.

MATERIALS AND METHODS

Materials

Dynabeads M-450 Epoxy (4.5 µm in diameter) were obtained from Thermo Fisher Scientific Inc. Poly(diallyldimethylammonium chloride) [PDADMAC; molecular weight (M_w) = 40,000 to 50,000] was purchased from Sigma-Aldrich Co. LLC. and used as received. PDMS (SYLGARD 184 Kit) was purchased from Dow Corning.

µWheel fabrication

To assemble and permanently link µwheel constituent particles, we placed a mixture of 20 µl of Dynabeads M-450 Epoxy (10 mg/ml) and 200 µl of 1% PDADMAC (M_w = 40,000 to 50,000) under an x-y planar rotating magnetic field (B_{xy} = 5 to 6 mT) at room temperature for 20 to 30 min. In this process, µwheels of differing size and structure were formed, each irreversibly bound due to bridging of the positively charged polyelectrolytes across negatively charged Dynabeads composing each wheel.

Topographic surface fabrication

We fabricated PDMS replicas of diffraction gratings (Thorlabs) of known spacing (100 lines/mm; no. GR2550-10106). In this, a commercially available PDMS two-component kit was used where a mixture of elastomer and curing agent (10:1) was poured over the grating and cured under vacuum for 60 min. Once cured, PDMS replicas were peeled from the masters and placed on a cleaned glass slide for use.

Magnetic field control

A 3D magnetic field was created with five air-cored copper solenoid coils (50 mm in inner diameter, 51 mm in length, and 400 turns with current capacity of 3.5 A) as shown in fig. S1A. Current signals controlled by MATLAB (MathWorks Inc.) and an output card (National Instruments, NI-9263) were amplified (KEPCO, BOP-40-5m) and then passed through those coils to generate the magnetic field. In-time signal monitoring was performed via a data card (National Instruments, NI-USB-6009) and Gaussmeter (VGM Gaussmeter, AlphaLab Inc.). µWheel propulsion was captured at a frame rate of 200 frames per second via charge-coupled device camera (EPIX Inc., SV643M) mounted on an inverted microscope (Olympus, IX 71).

SUPPLEMENTARY MATERIALS

robotics.sciencemag.org/cgi/content/full/4/32/eaaw9525/DC1
Materials and Methods
Fig. S1. Experimental setup and the rolling of a µwheel under a 3D magnetic field.
Fig. S2. µWheels translating on flat surfaces.
Fig. S3. Schematics for modeling the rolling of a dimer on a textured surface and textured surface with trapezoidal bumps used in the simulations.
Fig. S4. Calculation of an ideal road for a square (4,4) µwheel translating without slip.
Movie S1. Translation of a 7-mer and a 5-mer under a 3D magnetic field on a flat surface.
Movie S2. Translation of a dimer on a flat surface.
Movie S3. Translation of a dimer under a 3D magnetic field on a topographic surface along the blaze direction.
Movie S4. The simulated translation (slip and flip) of a dimer on a topographic surface with evenly spaced trapezoidal bumps.
Movie S5. The simulated translation (sequential flip of two lobes) of a dimer on a flat substrate.
Movie S6. The simulated translation (continuous flip) of dimer on a topographic surface with trapezoidal bumps spaced by d = 1.39a.
Movie S7. The rectifier effect for the translation of a dimer under a 3D magnetic field on a topographic surface.
Movie S8. Comparison of a diamond and square µwheel translation on the flat (top) versus topographic surface against the blaze direction (bottom).
Movie S9. Translation of a diamond and square against the blaze direction.

REFERENCES AND NOTES

1. J. Wang, W. Gao, Nano/microscale motors: biomedical opportunities and challenges. *ACS Nano* **6**, 5745–5751 (2012).
2. P. Erkoc, I. C. Yasa, H. Ceylan, O. Yasa, Y. Alapan, M. Sitti, Mobile microrobots for active therapeutic delivery. *Adv. Ther.* **2**, 1800064 (2019).
3. E. M. Purcell, Life at low Reynolds number. *Am. J. Phys.* **45**, 3–11 (1977).
4. P. Tierno, R. Muruganathan, T. M. Fischer, Viscoelasticity of dynamically self-assembled paramagnetic colloidal clusters. *Phys. Rev. Lett.* **98**, 028301 (2007).
5. A. C. H. Coughlan, M. A. Bevan, Rotating colloids in rotating magnetic fields: Dipolar relaxation and hydrodynamic coupling. *Phys. Rev. E* **94**, 042613 (2016).
6. R. Dreyfus, J. Baudry, M. L. Roper, M. Fermigier, H. A. Stone, J. Bibette, Microscopic artificial swimmers. *Nature* **437**, 862–865 (2005).
7. A. Ghosh, P. Fischer, Controlled propulsion of artificial magnetic nanostructured propellers. *Nano Lett.* **9**, 2243–2245 (2009).
8. L. Zhang, N. P. Sherlock, R. J. Meyer, T. R. Shrout, Artificial bacterial flagella: Fabrication and magnetic control. *Appl. Phys. Lett.* **94**, 162906 (2009).
9. S. Tottori, L. Zhang, F. Qiu, K. K. Krawczyk, A. Franco-Obregón, B. J. Nelson, Magnetic helical micromachines: Fabrication, controlled swimming, and cargo transport. *Adv. Mater.* **24**, 811–816 (2012).
10. C. E. Sing, L. Schmid, M. F. Schneider, T. Franke, A. Alexander-Katz, Controlled surface-induced flows from the motion of self-assembled colloidal walkers. *Proc. Natl. Acad. Sci. U.S.A.* **107**, 535–540 (2010).
11. M. Vilfan, A. Potočnik, B. Kavčič, N. Osterman, I. Poberaj, A. Vilfan, D. Babič, Self-assembled artificial cilia. *Proc. Natl. Acad. Sci. U.S.A.* **107**, 1844–1847 (2010).
12. F. Martinez-Pedrero, A. Ortiz-Ambriz, I. Pagonabarraga, P. Tierno, Colloidal microworms propelling via a cooperative hydrodynamic conveyor belt. *Phys. Rev. Lett.* **115**, 138301 (2015).
13. F. Martinez-Pedrero, P. Tierno, Magnetic propulsion of self-assembled colloidal carpets: Efficient cargo transport via a conveyor-belt effect. *Phys. Rev. Appl.* **3**, 051003 (2015).
14. T. O. Tasci, P. S. Herson, K. B. Neeves, D. W. M. Marr, Surface-enabled propulsion and control of colloidal microwheels. *Nat. Commun.* **7**, 10225 (2016).
15. M. Driscoll, B. Delmotte, M. Youssef, S. Sacanna, A. Donev, P. Chaikin, Unstable fronts and motile structures formed by microrollers. *Nat. Phys.* **13**, 375–379 (2017).
16. A. Kaiser, A. Snezhko, I. S. Aranson, Flocking ferromagnetic colloids. *Sci. Adv.* **3**, e1601469 (2017).
17. T. O. Tasci, D. Disharoon, R. M. Schoeman, K. Rana, P. S. Herson, D. W. M. Marr, K. B. Neeves, Enhanced fibrinolysis with magnetically powered colloidal microwheels. *Small* **13**, 1700954 (2017).
18. T. Yang, T. O. Tasci, K. B. Neeves, N. Wu, D. W. M. Marr, Magnetic microlassos for reversible cargo capture, transport, and release. *Langmuir* **33**, 5932–5937 (2017).
19. G. Kokot, A. Snezhko, Manipulation of emergent vortices in swarms of magnetic rollers. *Nat. Commun.* **9**, 2344 (2018).
20. H. Xie, M. Sun, X. Fan, Z. Lin, W. Chen, L. Wang, L. Dong, Q. He, Reconfigurable magnetic microrobot swarm: Multimode transformation, locomotion, and manipulation. *Sci. Robot.* **4**, eaav8006 (2019).
21. L. Hall, S. Wagon, Roads and wheels. *Math. Mag.* **65**, 283–301 (1992).
22. F. Kuczmarski, Roads and wheels, roulettes and pedals. *Am. Math. Mon.* **118**, 479–496 (2011).
23. A. Terray, J. Oakey, D. W. M. Marr, Microfluidic control using colloidal devices. *Science* **296**, 1841–1844 (2002).
24. T. Sawetzki, S. Rahmouni, C. Bechinger, D. W. M. Marr, In situ assembly of linked geometrically coupled microdevices. *Proc. Natl. Acad. Sci. U.S.A.* **105**, 20141–20145 (2008).
25. X. J. A. Janssen, A. J. Schellekens, K. van Ommering, L. J. van Ijzendoorn, M. W. J. Prins, Controlled torque on superparamagnetic beads for functional biosensors. *Biosens. Bioelectron.* **24**, 1937–1941 (2009).
26. P. Tierno, R. Golestanian, I. Pagonabarraga, F. Sagués, Controlled swimming in confined fluids of magnetically actuated colloidal rotors. *Phys. Rev. Lett.* **101**, 218304 (2008).
27. P. Tierno, O. Güell, F. Sagués, R. Golestanian, I. Pagonabarraga, Controlled propulsion in viscous fluids of magnetically actuated colloidal doublets. *Phys. Rev. E* **81**, 011402 (2010).
28. H. Faxen, Die Bewegung einer starren Kugel langs der Achse eines mit zaher Flussigkeit gefullten Rohres: Arkiv for Matemetik. *Astronomi och Fysik* **17**, 1–28 (1923).
29. H. Brenner, The slow motion of a sphere through a viscous fluid towards a plane surface. *Chem. Eng. Sci.* **16**, 242–251 (1961).
30. A. J. Goldman, R. G. Cox, H. Brenner, Slow viscous motion of a sphere parallel to a plane wall—I Motion through a quiescent fluid. *Chem. Eng. Sci.* **22**, 637–651 (1967).
31. B. Cichocki, R. B. Jones, Image representation of a spherical particle near a hard wall. *Physica A* **258**, 273–302 (1998).
32. S. H. Rad, A. Najafi, Hydrodynamic interactions of spherical particles in a fluid confined by a rough no-slip wall. *Phys. Rev. E* **82**, 036305 (2010).
33. M. M. Rashidi, S. Johnson, Z. Yang, Theoretical study of moving magnetic beads on an inclined plane and its application in the ratchet separation technique. *J. Magn. Magn. Mater.* **398**, 13–19 (2016).
34. G. Helgesen, Magnetic propulsion of microspheres at liquid-glass interfaces. *J. Appl. Phys.* **123**, 064902 (2018).
35. C. F. Chou, O. Bakajin, S. W. P. Turner, T. A. J. Duke, S. S. Chan, E. C. Cox, H. G. Craighead, R. H. Austin, Sorting by diffusion: An asymmetric obstacle course for continuous molecular separation. *Proc. Natl. Acad. Sci. U.S.A.* **96**, 13762–13765 (1999).
36. M. P. MacDonald, G. C. Spalding, K. Dholakia, Microfluidic sorting in an optical lattice. *Nature* **426**, 421–424 (2003).
37. L. R. Huang, E. C. Cox, R. H. Austin, J. C. Sturm, Continuous particle separation through deterministic lateral displacement. *Science* **304**, 987–990 (2004).

Funding: T.Y., N.W., and D.W.M.M. acknowledge financial support from the National Aeronautics and Space Administration (grant no. NNX13AQ54G). K.B.N. and D.W.M.M. also thank the National Institutes of Health under grants R21NS082933 and R01NS102465. **Author contributions:** T.Y. and A.T. performed the experiments. T.O.T. designed the μwheel binding and wrote custom codes. T.Y. and T.O.T. built the experimental setups. K.B.N., N.W., and D.W.M.M. conceived the project. T.Y., K.B.N., N.W., and D.W.M.M. analyzed the experimental results and wrote the manuscript. **Competing interests:** The authors declare that they have no competing interests. **Data and materials availability:** All data needed to support the conclusions of this manuscript are included in the main text or Supplementary Materials.

Submitted 8 February 2019
Accepted 24 June 2019
Published 31 July 2019
10.1126/scirobotics.aaw9525

Citation: T. Yang, A. Tomaka, T. O. Tasci, K. B. Neeves, N. Wu, D. W. M. Marr, Microwheels on microroads: Enhanced translation on topographic surfaces. *Sci. Robot.* **4**, eaaw9525 (2019).

Science Robotics

Microwheels on microroads: Enhanced translation on topographic surfaces

Tao Yang, Andrew Tomaka, Tonguc O. Tasci, Keith B. Neeves, Ning Wu, and David W. M. Marr

Sci. Robot. **4** (32), eaaw9525. DOI: 10.1126/scirobotics.aaw9525

Science Robotics (ISSN 2470-9476) is published by the American Association for the Advancement of Science. 1200 New York Avenue NW, Washington, DC 20005. The title *Science Robotics* is a registered trademark of AAAS.